Detection of haemorrhagic stroke in simulation and realistic 3-D human head phantom using microwave imaging

Behnaz Sohani[a,*], Banafsheh Khalesi[a], Navid Ghavami[b], Mohammad Ghavami[a], Sandra Dudley[a],
Amir Rahmani[c], Gianluigi Tiberi[a,b]

[a] *School of Engineering, London South Bank University, London, UK.*
[b] *UBT-Umbria Bioengineering Technologies, Perugia, Italy.*
[c] *Castlet Ltd, Lincoln, UK.*

Abstract

This research presents the use and validation of a low complexity microwave imaging procedure for brain imaging, where antennas operate in free-space. In particular, we employ only two microstrip antennas, operating between 1 and 2 GHz for successful detection of the haemorrhagic stroke. Detection is demonstrated through simulation and measurements. Simulations have been performed using an anthropomorphic human head model where a haemorrhagic stroke has been inserted. In addition, multi-bistatic frequency-domain measurements have been performed to collect the transfer function (S21) between the two antennas inside an anechoic chamber using a multi-layered phantom mimicking a human head. Images have been obtained through Huygens principle. To reconstruct the image, subtraction artefact removal method between the data of a healthy head and the data of a head with stroke has been initially employed in simulations. Next, the rotation subtraction artefact removal method has been used both in simulation and in measurements. It has been verified that both artefact removal procedures allow detection.

Keywords: Microwave imaging, Brain stroke detection, haemorrhagic stroke detection, Huygens principle.

1. Introduction

Severe brain injuries include acquired and traumatic injuries that are caused by external forces (such as falls or accidents) or internal incidences (such as stroke and tumours). Brain strokes occur when cerebral blood circulation fails as a result of a blocked or burst blood vessel, causing an ischemia or a haemorrhage, respectively. There are common symptoms between the transient ischemic attack (TIA), strokes and generic medical conditions like fainting, migraine, heart problems and seizures [1]. Therefore, the other health conditions should not be misdiagnosed with stroke. It is well known that providing immediate medical attention for a patient with a brain injury is of vital importance. Every second, from the moment of brain injury, millions of brain cells die, leading to irreparable and permanent damage or even death. Thus, if medical staff diagnose stroke, and perform an appropriate drug treatment within a few hours of the symptoms onset, they play a crucial role in saving a patient's life [2]. Hence, a portable diagnosis system is pivotal on the spot for rapid diagnosis of brain injuries. Initially, a clinical examination using a neurological assessment is performed by a general practitioner (GP) [2]. However, this assessment cannot prove a definite conclusion as many non-vascular conditions can appear as stroke symptoms. As such, medical professionals rely on the computed tomography (CT) scan and on the magnetic resonance imaging (MRI) in the process of diagnosis. They are however, neither fast nor portable (owing to pertinent dimensions of the devices), and are not utilisable at small medical centres. Compared to CT and MRI scanners, microwave imaging (MWI) can provide a portable detection system, and allow initial diagnosis of various emergency life-threatening

---

[*] Corresponding author

circumstances such as strokes due to brain injury, whilst patients are still being taken by ambulance to a hospital, saving critical time [3].

MWI for brain abnormalities has recently been proposed [4, 5] and exploits the differences in tissues' dielectric properties [5]. It has been demonstrated that haemorrhagic stroke changes the dielectric properties of the tissues [6]. Haemorrhagic stroke results in a significant increase in the dielectric properties (up to 20%) with respect to the dielectric properties of white/grey matter [7], while ischemic stroke leads to a decrease in the dielectric properties with respect to that of the white/grey matter [4, 8]. MWI can be divided into radar techniques and microwave tomography [9]. Microwave tomography endeavours to reconstruct the dielectric property profile of the head by finding a solution to a relatively nonlinear and ill-posed inverse scattering problem [10, 11]. One of the detrimental points of microwave tomography is the solution instability resulted from the complex mathematical formulations. In contrast, radar imaging entails finding a solution to a simpler problem of discovering the scattering map based on contrast amongst the dielectric properties. Examples of such radar imaging technique have been proposed [12]. From the hardware point of view, a difficulty of MWI technology is how to conform more antennas together to coat the region of human tissues to be investigated [13]. The coupling medium can optimise antenna penetration, however, with great complexity [14]. In addition, the antenna is required to be immersed in a 90% glycerine-water mixture to achieve broadband operation and couple energy more efficiently into the head [15]. With the aim of lowering hardware complexity, in this paper we propose to employ only one transmitting antenna and one receiving antenna (coupled through a vector network analyser (VNA)), both operating in free space. The antennas rotate all around the object in order to collect the signals in a multi-bistatic fashion. Next, an algorithm based on Huygens principle (HP) is used to localise strong scatterers (similar to radar imaging). In more detail, the HP based technique allows the detection of dielectric inhomogeneities in the frequency domain [16, 17]. Hitherto, HP has been exploited for several cancer detection applications, notably for breast and skin cancer detection [18- 20]. The procedure permits to distinguish between different tissues, or different conditions of tissues, and to get a final image, which represents a homogeneity map of the dielectric properties (dielectric constant and/or conductivity). In this paper, we will assess the capability of the proposed procedure in detecting haemorrhagic stroke (only) through both simulations and measurements. In order to detect the haemorrhagic stroke inside a multi-layered head phantom, two specifically designed and fabricated wideband (WB) antennas are used as the transmitting and receiving antennas using MWI technique based on HP.

The rest of this paper is organised as fallows. The next section explains the simulation model, and the procedures employed in the imaging procedure. Also, this section describes the fabrication procedure of head phantom and the frequency-domain measurements. In section 3, we present the results obtained. Finally, section 4 discusses and concludes the simulation and experimental results.

2. Materials and methods

2.1. Antenna design and simulation

This section details the design and fabrication of a WB microstrip antenna operating between 1 and 2 GHz. This band has shown to be optimal for brain imaging [3]; in addition, it is clearly highlighted that WB can enhance performance in lesion detection [21]. Therefore, a WB antenna which works efficiently across that band is a vital factor on the success of the suggested system. We are proposing an effective technique for increasing the bandwidth of the antenna and subsequently a better head image through designing an isosceles triangular patch antenna using fractal ground plain. Building on this work, the initial idea of using fractal ground plane technique has drawn inspiration from [22, 23]. The antenna has been modelled in CST Microwave studio. It is designed and fabricated using FR-4 substrate material with a dielectric constant of $\epsilon_r = 4.7$. The 50 Ω discrete microstrip feeding structure is used at the bottom part of the patch. The proposed microstrip antenna has a single-layer structure and consists of four parts: Triangular patch and microstrip feed line, substrate and fractal ground plane. Fig. 1 shows the fabricated antenna for our envisioned brain imaging scanner. The patch geometry is isosceles triangular shape. Also, the antenna is fed using an SMA connector, connected with a transmission line as shown in Fig. 1.

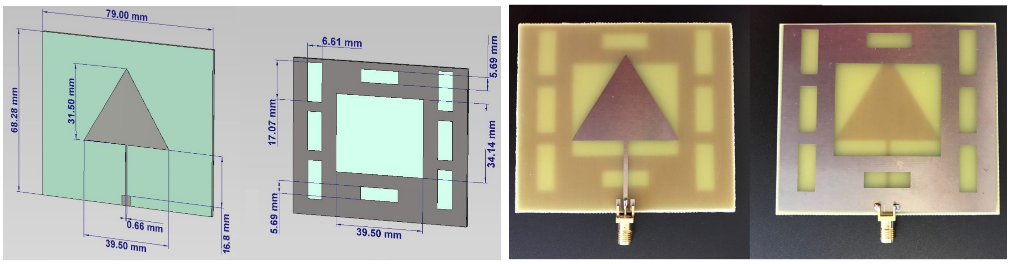

(a) **(b)** **(a)** **(b)**

Figure 1: The designed triangular patch microstrip antenna and the fabricated antennas with fractal ground plane: (a) front, (b) back.

The impedance bandwidth of the antenna is improved by optimizing the slot shape and dimensions in the ground and the triangular antenna structure. Also, a fractal ground can be appropriately designed to ensure WB operation. The simulated antenna is considered both in free space and near a head model. A 3D model consisting of head tissues of the Ella model (ITIS Foundation, Switzerland) is employed with 2mm × 2mm × 2mm isotropic resolution, as shown in Fig. 2, where the antenna is positioned with its isosceles triangle axis of symmetry parallel to the y-axis of the reference system. The Ella model provides details of electric conductivity and relative permittivity for the different tissues of a young and healthy female at the age of 26 [24, 25].

To simulate the existence of a haemorrhagic stroke inside the head model, we have considered a spherical region with the dielectric properties of blood, with radius of 10 mm, relative permittivity and conductivity of 60 and 1.79 S/m at 1.6 GHz, respectively in the head model [24, 25]. The transmitting antenna has been placed 17 cm away from the centre of the Ella model's head. The proposed triangular antenna has been fabricated in-house at London South Bank University (LSBU) (as shown in Fig. 1) and the correspondent S11 (input port voltage reflection coefficient) measurements have been taken in the anechoic chamber, both in free-space and in front of a human head using a vector network analyser (Anritsu MS2028C VNA Master manufactured by Anritsu EMEA Ltd). Fig. 3 demonstrates the measured and simulated scatter parameter S11 for the proposed antenna both near the head and in free space. As shown in Fig. 3(a), the operational frequency is 1.6 GHz with a bandwidth >10%.

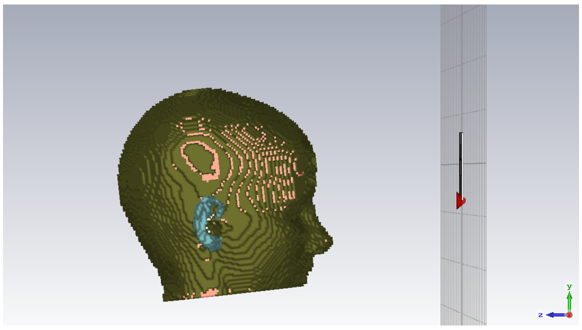

Figure 2: The simulated antenna and 3D head of the Ella model (ITIS Foundation, Switzerland) using CST software. The antenna is positioned with its isosceles triangle axis of symmetry parallel to the y-axis of the reference system; Ella model is positioned with its longitudinal axis parallel to the y-axis of the reference system.

The measured S11 both in front of human head and in free space indicates excellent agreement with the simulation results, as shown in Fig. 3. In addition, measurements reveal that matching and bandwidth slightly increase in the presence of the human head. Furthermore, an operational bandwidth greater than 10% centred at 1.6 GHz makes this antenna an ideal candidate for brain imaging experiments. In fact, it has

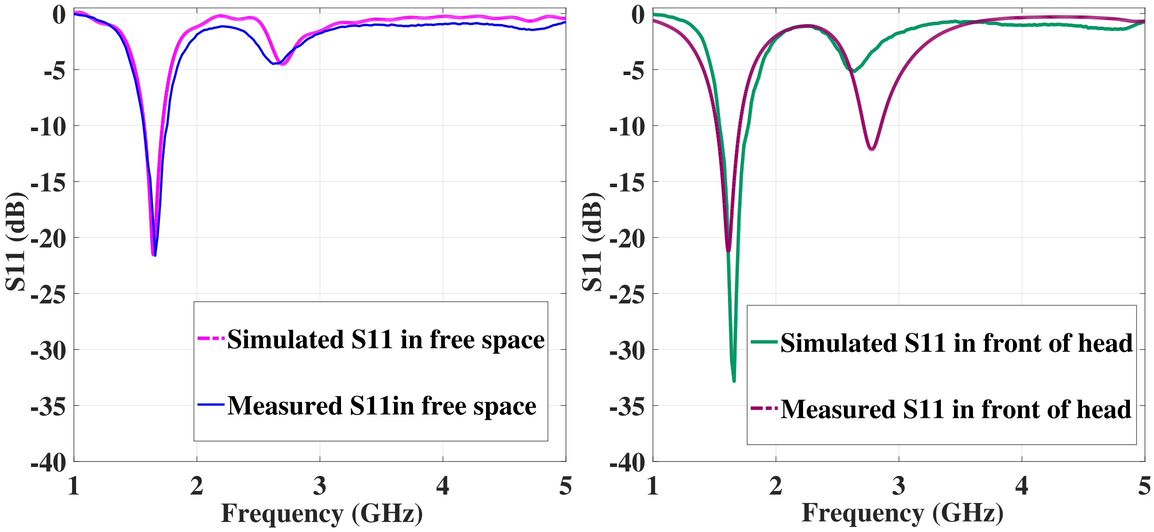

Figure 3: Simulated and measured reflection coefficient S11 of the patch antenna: (a) in free space and, (b) in front of human head.

been shown that higher frequencies are not suitable for brain imaging due to the high signal attenuation, while lower frequencies decrease the resolution [21].

In order to provide the corresponding initial data and results which are then used in section 3 for imaging, different working steps have to be performed. First, the simulation has been done for two different situations, i.e. for a healthy head model which is mentioned before as Ella model and a head model with a spherical emulated haemorrhagic stroke, and for four different positions of the antenna with respect to Ella model. It should be pointed out that, rather than rotating Ella model around its longitudinal axis, the four different positions from the angles of 0°, 5°, 40° and 45°, have been synthetised by rotating the microstrip patch antenna. Fig. 4 displays the magnitude of y-component of the electric field on an xz-plane for: (a) Ella model (abbreviated as Ey), (b) when the emulated stroke is included in the Ella model (denoted as Ey-WSTR) and (c) the difference between the Ella model and the Ella model with stroke (abbreviated as dEy). Moreover, the y-component of the electric field on one external surface of the head is calculated and used for performing the imaging, as shown in section 3. It should be pointed out that only the y-component of the electric field will be used for performing the imaging, due to x and z components vanishing. Specifically, the y-component of the electric field is calculated on a circular grid of points with radius of 110 mm and 6° phi sampling just outside the Ella head model. In Fig. 4, the external ellipse with white dots represents the head contour, while the haemorrhagic stroke area is the yellow region at the bottom left of the head (located at frontal lobe of the head model) in Fig. 4 (c).

2.2. Phantom Fabrication

2.2.1. Phantom Material Production

To experimentally validate a procedure for microwave explorations on the brain haemorrhages, a realistic phantom is required. A realistic phantom described in the literature [26] has concentrated mainly on a close similarity to the physical features of the head rather than to the actual dielectric properties. In this study [26], a substance with permittivity of 6 was employed to represent the exterior skull tissues including the bone. The phantom proposed in this paper is instead primarily based on a close similarity to the real dielectric properties of the head tissues. To achieve feasible fabrication, the phantom has been fabricated using three layers, which mimics: I) skull bone with realistic dielectric properties of cancellous and cortical bone, II) a combination of grey matter and white matter, III) blood inclusion. The suggested phantom is designed to mimic the skull bone with a thickness of roughly 10 mm, equivalent conductivity of 0.24 S/m and relative permittivity of 12 at 1.6 GHz. These values are presumed to provide an average value

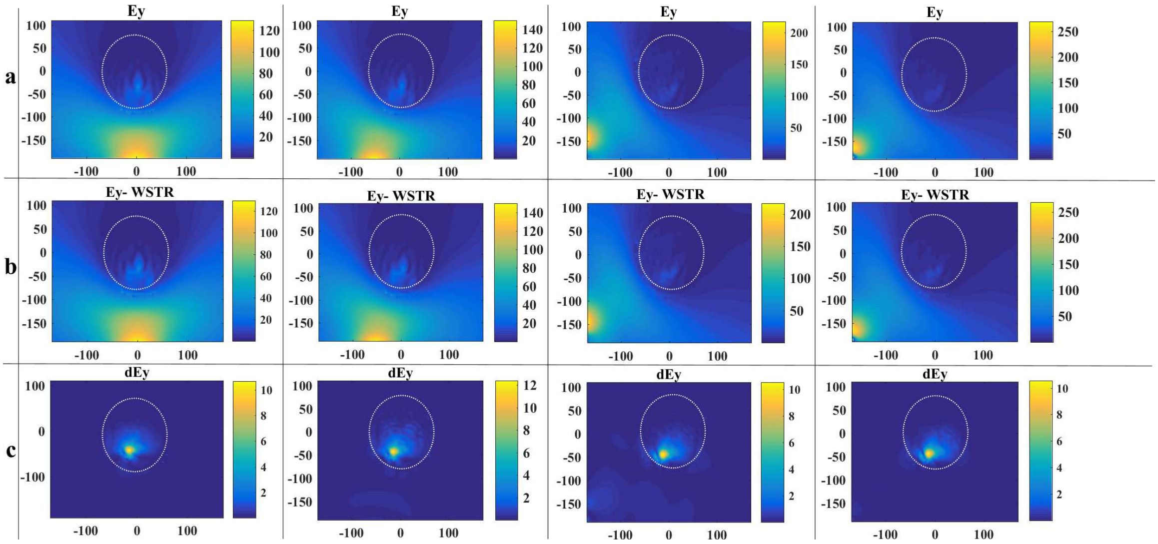

Figure 4: The y-component electric fields on an xz-plane from the angles of 0°, 5°, 40° and 45° for; (a) the Ella model, (b) when the emulated stroke is included in the Ella model and (c) the difference between the Ella model and the Ella model with stroke. The vertical colour-bar at the right of each figure indicates the intensity of the electric field (in V/m). Both x and z axes show the distance in millimetres.

for the cancellous and cortical bone. In contact with the inner layer of the skull bone, there is dominating grey and white matter with an average conductivity of 1.01 S/m and permittivity of 44 at 1.6 GHz. Blood provides a contrast through its conductivity of 1.79 S/m and permittivity of 60 at 1.6 GHz. The dielectric constant of each layer is given in Table 1, where the values have been derived from [24], [25], and [27]. To simulate the dielectric properties of the head and brain stroke tissues, different materials were used in order to approximate the values reported. The suggested phantom contains a solid representing skull filled with two combinations of liquids mimicking grey/white matter and the blood (haemorrhagic stroke). Moreover, the selection of ingredients was driven by some further advantageous factors such as the low cost of materials, the ease of access (off-the-shelf) and the stability over long periods of storage time.

Table 1: Dielectric constant and conductivity at the frequency of 1.6 GHz [3], [24] and [25].

Tissue	**Relative Permittivity**	**Conductivity**
Realistic human brain (combination of grey matter and white matter)	44	1.01 S/m
Skull	12	0.24 S/m
Blood	60	1.79 S/m

Owing to the empirical use of only the top half of the head, a plain hemi-ellipsoidal shape with external horizontal axial diameters of 210 mm (back to front) and 195 mm (sideways), with height of 120 mm, was selected. Moreover, the brain mould filled with white matter and grey matter equivalent material has horizontal axial diameters of 190 mm (back to front) and 165 mm (sideways), and height of 90 mm. A small tube containing blood equivalent material with circular cross-sectional radius of 5 mm and a height of 35 mm is situated inside the brain mould. As Fig. 5 shows, three different volumes of container are subsequently placed inside each other. Each layer of the head phantom has been fabricated using mixtures of the constituent materials with the proper ratios. The recipes for producing different mixtures are summarised in Table 2 [27, 28].

In the combination suggested in Table 2, deionised water is employed as the principal substance or source of permittivity, as it displays high dielectric values over a wide bandwidth. Sugar, salt, sunflower oil and corn flour are employed to control the relative permittivity of the compounds. The method employed at the

Table 2: Tissue mimicking recipes.

	Corn Flour (%)	**NaCl Salt (%)**	**Oil (%)**	**Sugar (%)**	**Glycerine (%)**	**DI Water (%)**
Skull	47.29	0.26	30.09	9.46	0.00	12.90
GM / WM (Brain)	0.00	0.00	0.00	0.00	40.00	60.00
Blood	0.00	0.00	0.00	0.00	15.00	85.00

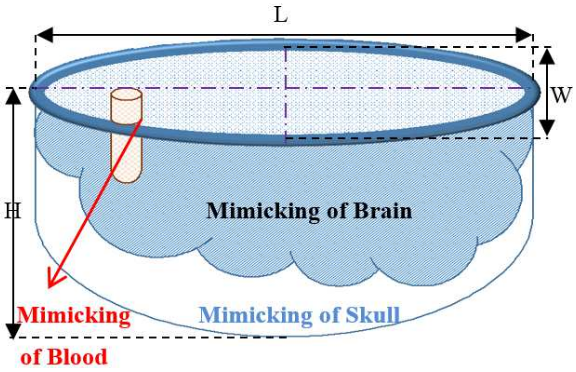

Figure 5: Design of different layers of phantom.

time of material fabrication is as follows.
I. Blood mimicking tissue:
-The blood has been mimicked using a combination of deionised water and glycerine with ratios of 15% and 85%, respectively.
II. Brain mimicking tissue:
-In the mixing bowl, stir a combination of deionised water and glycerine with ratios of 40% and 60%, respectively.
III. Skull mimicking tissue:
-In a small beaker, mix the corn flour and oil (in more details, sunflower oil) together and beat into a smooth batter with no dry clumps of flour. Then, in another beaker, mix deionised water with sugar/salt and stir until the sugar/salt were completely dissolved in the water. Combine the two mentioned mixes until it formed a uniform shape.
-Then, in another beaker, mix deionised water with sugar/salt and stir until the sugar/salt were completely dissolved in the water.
-Combine the two mentioned mixes until it formed a uniform shape.

In this step, skull equivalent ingredients have been poured in to perfectly fill the gaps surrounding the brain and the blood, as shown in Fig. 6.

Figure 6: The fabricated head phantom.

The dielectric properties of the skull mimicking tissue's mixture were measured employing the Epsilon dielectric measurement device (Biox Epsilon Model E100 fabricated at Biox System Company Ltd) and for the mixtures of brain and blood mimicking tissue, the dielectric probe (Keysight technologies, M9370A), connected to a network analyser was used to measure the electrical properties at room temperature. The Epsilon is a device for contact measurement using a fingerprint sensor which reacts to capacitance. It is useful for measurements on isolated soft liquids and solids. It is worth mentioning that this device cannot provide the dielectric value at the frequency of interest, but can provide the permittivity values at frequency of 0 Hz. Nevertheless, this is appropriate for a material which is made up of constituents that do not experience any changes with frequency variation, such as flour and oil. Since the skull mimicking tissue comprises mainly a high percentage of corn flour and sunflower oil, the obtained measured permittivity with this device at 0 Hz frequency has been considered equivalent to its permittivity at a frequency of 1.6 GHz. This does not hold true for brain and stroke recipes that are fabricated chiefly by a high percentage of glycerine.

2.2.2. Measurements inside an Anechoic Chamber

Frequency domain measurements have been carried out inside an anechoic chamber, to gather the transfer function S21 between the two antennas through a VNA. The fabricated antennas, vertically polarised, were used, after calibration. In more detail, the transmitting antenna was connected to port 1 of the VNA and the receiving antenna connected to port 2 of the VNA; S21 is the parameter representing the complex transfer function from the transmitting antenna to the receiving antenna. The prepared phantom was positioned at the centre of a rotating table. Fig. 7 shows the phantom and fabricated antennas inside the anechoic chamber.

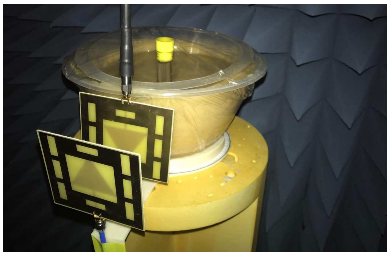

Figure 7: Phantom's position inside the anechoic chamber.

The multilayer phantom contains a target inclusion having specific conductivity and/or permittivity of blood. The aim is to find the existence and location of the target, using the measured field of the receiving antenna, which is collected at many points r_{xn} placed all around the phantom surface. Through both simulations and measurements, it has been verified that the field reconstructed in the medium under test will display a mismatch around the transition region of the two media, which is where the target is positioned [18]. This mismatch permits detection. Fig. 8 depicts the sketch of the measurement setup, where the hemi-ellipsoidal shape phantom of the head is shown in light blue. The black and green dashed circles indicate the perimeter where the transmitting and receiving antennas can be moved circularly on the azimuthal plane, in order to irradiate and thereafter receive the signals from different directions. The antennas are at the same height. For each set of measurements, the transmitting antenna has been placed 17 cm away from the centre of the rotating table, the same way it was done in simulations. For each transmitting position, we recorded the S21 at $N_{PT} = 60$ receiving positions. Specifically, we measure S21 at the points $rx_{np} \equiv (a_0; \phi_{np}) \equiv \overrightarrow{\rho}_{np}$, displaced along a circular surface having radius a_0. a_0 is the distance between the centre of the rotating table and the receiving antenna (also shown in Fig. 7) which is 14 cm [21]:

$$S21_{\mathrm{t}x_m}|_{\mathrm{r}x_{np}} = S21_{np,\mathrm{t}x_m} \quad \text{with} \quad np = 1, ..., N_{\mathrm{PT}} \tag{1}$$

Subscript m indicates the transmitting positions tx and np=1, 2, ..., N_{PT} the receiving positions. It must be emphasized that, instead of moving the transmitting antenna here, the transmitting positions are synthesised by suitably rotating the phantom. A total number of 8 transmitting positions have been synthesises (m=1,...,8), divided in four doublets displaced 90°, with each doublet consisting of two closest transmitting positions displaced 5° from each other. To summarize, the following transmitting positions have been synthesised: 0° and 5°, 90° and 95°, 180° and 185°, 270° and 275°. For the purpose of exploiting how the signals vary at different frequencies, complex S21 values were recorded over a full range of frequency between 1 and 2 GHz, using a frequency sample spacing of 5 MHz.

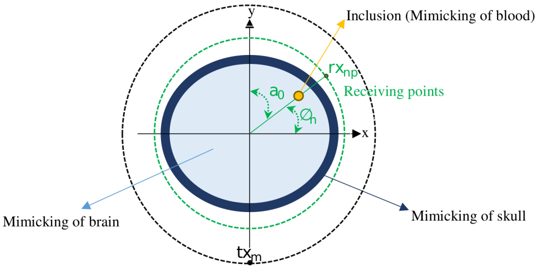

Figure 8: Pictorial view of the measurement.

2.3. *Imaging procedure*

We consider what happens if HP is employed for reconstruction of the medium's internal field, employing the field simulated or measured on its external surface as the locus of a wave. More in details, we calculate the superposition of the fields radiated by NPT receiving points of eq. (1):

$$E_{\mathrm{HP,2D}}^{\mathrm{rcstr}}(\rho,\phi;\mathrm{tx}_m;f)=\Delta_s\sum_{np=1}^{N_{PT}}S21_{np,\mathrm{tx}_m}G(k_1|\overrightarrow{\rho}_{np}-\overrightarrow{\rho}|) \tag{2}$$

where $\overrightarrow{\rho}\equiv(\rho,\phi)$ indicates the observation point; k_1 is the medium's wave number in the imaging zone; and Δ_s represents the spatial sampling. In $E_{\mathrm{HP,2D}}^{\mathrm{rcstr}}$, the string rcstr indicates the "reconstructed" internal electric field, and the string HP indicates that a HP based procedure is to be used. Furthermore, it is noted that the reconstructed electric field depends on both frequency and illuminating source. In eq. (2), the Green's function G for homogenous media is employed to propagate the field. Suppose that we employ N_F frequenciesf_i, then the final image's intensity (I) is achieved through eq. (3), i.e. by incoherent addition of all the solutions [29]:

$$I(\rho,\phi)=\sum_{i=1}^{N_F}|E_{\mathrm{HP}}^{\mathrm{rcstr}}(\rho,\phi;\mathrm{tx}_m;f_i)|^2 \tag{3}$$

Signal pre-processing techniques are usually used to reduce artefacts, which may be due to the direct fields and the fields reflected by the first layer. If the artefact is not removed successfully, it could mask strokes. To remove the artefact, we use two different methods: first, the subtraction between the data of a healthy head model (Ella) and the data of a head model with stroke; second, the rotation subtraction between different transmitting positions.

2.3.1. *Artefact removal algorithms: Subtraction*

In this method, the artefact removal has been achieved by subtracting the electric field (calculated on the circular grid of points with radius of 110 mm and 6° phi sampling just outside the head) for Ella with a stroke and for Ella without stroke.

2.3.2. Artefact removal algorithms: Rotation Subtraction

In the rotation subtraction method [30], artefact is removed by performing the subtraction between two sets of data obtained by slightly rotating the position of the transmitting antenna around the object. Referring to the notation used in Section 2.3, we can employ the following equation:

$$S21_{\mathrm{np},tx_{Diff}} = S21_{np,\mathrm{tx}_1} - S21_{np,\mathrm{tx}_2} \tag{4}$$

where tx_1 and tx_2 represent the two closest transmitting positions. The rotation subtraction artefact removal method may be applied to both simulation and measurements.

2.4. Image Quantification

Images may contain some clutter even following artefact removal procedures. Thus, it is appropriate to introduce a parameter in order to quantify and compare the performance in detection when using different artefact removal algorithms. The parameter which will be introduced is the signal-to-clutter ratio (S/C). Here, S/C is defined as the ratio between maximum intensity evaluated in the region of the lesion divided by the maximum intensity outside the region of the lesion [31]. The S/C ratio is calculated for each image, considering both artefact removal methods.

3. Results

3.1. Imaging through simulations

The images through simulation, obtained using both subtraction and rotation subtraction artefact removal methods, are shown in Fig. 9 and Fig. 10. Specifically, Fig. 9 shows the images (normalised to the maximum) obtained through eq. (3) after subtraction artefact removal procedure for the four different transmitting positions (0°, 5°, 40° and 45°). The correspondent S/C is given in Table 4. It is important to point out that all the images shown here and in the following sub-sections were normalised and adjusted, forcing the intensity values below 0.5 to zero, while S/C was always calculated before performing the image adjustment.

In Fig. 10, the images of the head model with a haemorrhagic stroke are shown applying the rotation subtraction artefact removal procedure to simulated data, using the transmitting set 0°, 5° (left) and the transmitting set 40°, 45° (right). The correspondent S/C is given in Table 5.

3.2. Phantom Imaging

Since the brain and blood mimicking tissues contain glycerine and water, the dielectric probe has been used here for measuring the dielectric properties, which are given in Table 3. As evident from the outcomes, a great agreement can be seen between the values reported in Table 3 and the corresponding values presented in Table 1. Fig. 11 shows the microwave images of the phantom obtained through eq. (3), after applying rotation subtraction artefact removal to the four doublets (0° and 5°; 90° and 95°; 180° and 185°; 270° and 275°), separately. The correspondent S/C is given in Table 6.

Table 3: Obtained permittivity and conductivity values at the frequency of 1.6 GHz for each layer of phantom.

Tissue	**Relative permittivity**	**Conductivity**
Mimicking of the Brain (combination of grey matter and white matter)	44.75	1.05 S/m
Mimicking of the Skull	12	–
Mimicking of the Blood	61.1	1.58 S/m

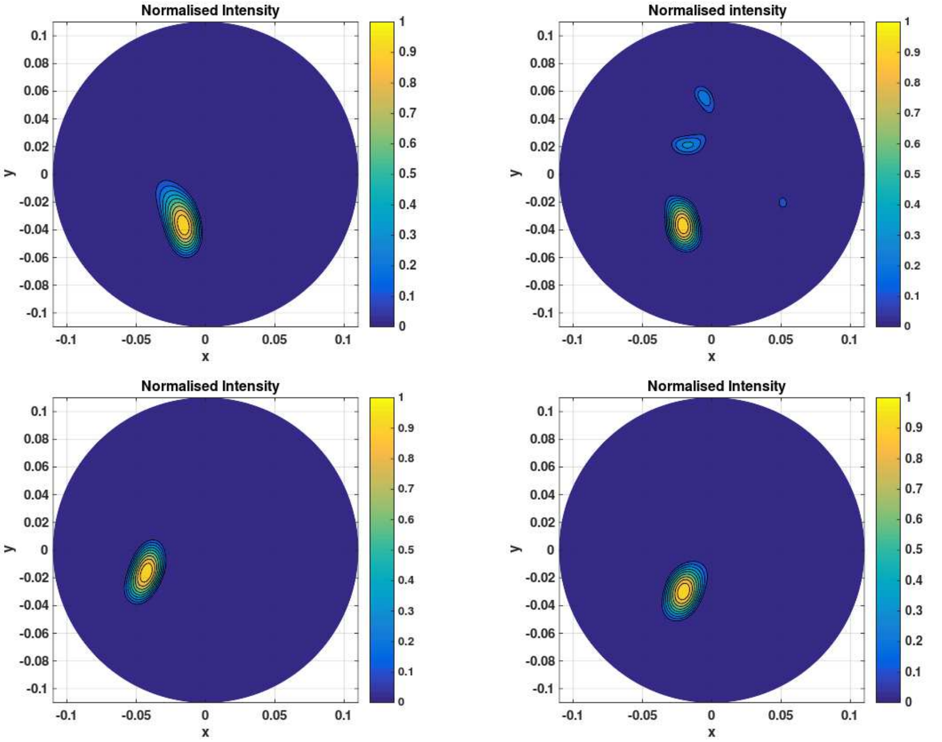

Figure 9: Images obtained using simulated data after performing artefact removal through subtraction, i.e. subtracting the electric fields of Ella with a haemorrhagic stroke (calculated on a circular grid of points displaced just outside the head) and Ella without the stroke (calculated on the same grid of points). For performing subtraction, the position of the transmitting antenna has been kept fixed. The 4 images refer to the 4 different positions of the transmitting antenna used in the simulation. Images are displayed following normalisation to the maximum value and converting intensity values lower than 0.5 to 0. X and y axes are in meters, while the intensity has an arbitrary unit.

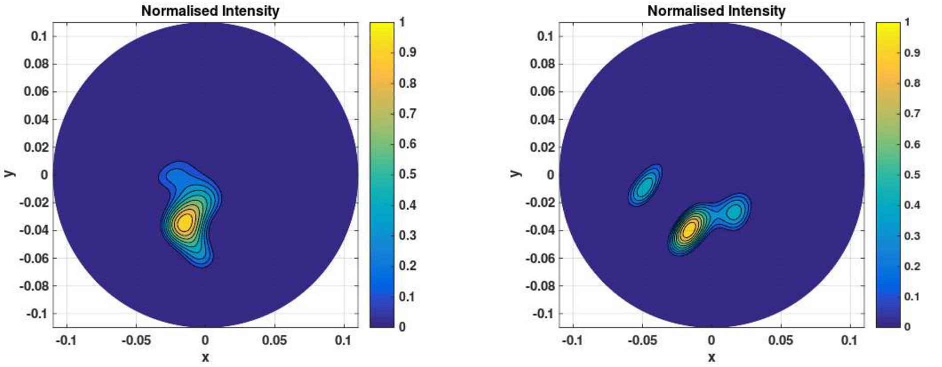

Figure 10: Images obtained using simulated data after performing artefact removal through rotation subtraction, i.e. subtracting two sets of data obtained by slightly rotating the position of the transmitting antenna around Ella with a haemorrhagic stroke. Images are displayed following normalisation to the maximum value and converting intensity values lower than 0.5 to 0. X and y axes are in meters, while the intensity has an arbitrary unit.

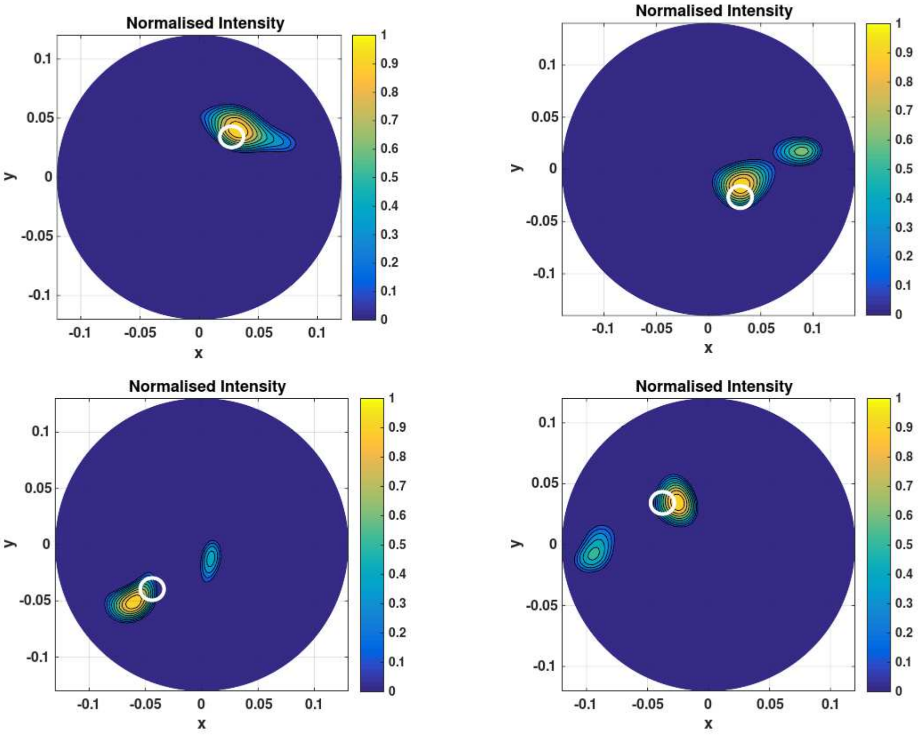

Figure 11: Images obtained using measured data after performing artefact removal through rotation subtraction, i.e. subtracting four pairs of data obtained by slightly rotating the position of the transmitting antenna around the phantom with inclusion. Images are displayed following normalisation to the maximum value and converting intensity values lower than 0.5 to 0. X and y axes are in meters, while the intensity has an arbitrary unit. The white circles represent the actual location of the inclusion mimicking the haemorrhagic stroke inside the head phantom.

Table 4: Within-brain S/C (linear) at the frequency of 1.6 GHz (using simulation and subtraction).

Positions	**Within-Brain S/C (linear) Subtraction**
Position 0°	2.5
Position 5°	1.91
Position 40°	1.93
Position 45°	2.49

Table 5: Within-brain S/C (linear) at the frequency of 1.6 GHz (using simulation and rotation subtraction).

Positions	**Within-Brain S/C (linear) Rotation Subtraction**
Position 0° - Position 5°	1.53
Position 40° - Position 45°	1.60

Table 6: S/C (linear) at the frequency of 1.6 GHz (using measurements and rotation subtraction).

Positions	**S/C (linear) Rotation Subtraction**
Position 0° - Position 5°	1.85
Position 90° - Position 95°	1.48
Position 180° - Position 185°	1.63
Position 270° - Position 275°	1.50

4. Discussions and Conclusions

In this paper, we simulated, fabricated and used WB antennas and employed a HP-based microwave imaging technique to detect haemorrhagic stroke in multi-layered head phantom. The simplicity of HP obviates the need for finding a solution to the inverse problems when forward propagating the waves. Additionally, the methodology of HP allows capturing the contrast such that different material properties within the region of interest could be detected in the final image. Haemorrhagic stroke detection has been achieved both in simulations and measurements, after using appropriate artefact removal algorithms to pre-process the signals. A large number of such existing artefact removal algorithms work on the basis of the simplified assumptions regarding the degree of commonality in the artefacts across all receiving channels. A wide spectrum of current artefact removal algorithms, coupled with algorithms altered from ground penetrating radar applications, are provided for comparison with a variety of suitable performance metrics [32]. The methods of artefact removal used in this paper were basically derived from the literature of [32]. The subtraction of the data between a healthy head model and a head model with haemorrhagic stroke has been employed in simulation, while rotation subtraction artefact removal has been employed in both simulation and measurements. It is worthwhile pointing out that, in a realistic scenario, only rotation subtraction artefact removal can be employed. The parameter S/C has been introduced to quantify the detection capability and thus, the performance of artefact removal algorithm. The highest value of S/C is obtained when employing the subtraction of the data between a healthy head model and a head model with haemorrhagic stroke, in simulation. More in details, as given in Table 4, the maximum S/C value is 2.5 (linear scale). When employing the rotation subtraction artefact removal to both simulated and measured data, a decrease in S/C can be observed, with a minimum value of 1.48 (linear scale), as given in Table 6. If follows that the use of the rotation subtraction artefact removal, in a realistic scenario, implies a S/C reduction of less than 3 dB with respect to the ideal case of performing artefact removal through subtraction between a healthy head and a head with haemorrhagic stroke. Recently, various system prototypes using microwaves for brain stroke diagnostics have been suggested. One example is the Stroke-finder, developed at Chalmers University [33], which detects and classifies different types of intracranial bleedings (ischemic or haemorrhagic). The device is comprised of 12 Tx/Rx triangular patch antennas fixed on a helmet made of plastic. The plastic balloons filled with water, between the head and the patch antennas, are used to act as matching medium. Another system, the BRIM G2 has been developed at EMTensor [34] for brain imaging. This system is comprised of 177 rectangular ceramic-loaded waveguide antennas fixed on a hemispherical stainless-steel chamber. The antennas are spaced evenly at eight rings, with different heights. Moreover, these rectangular antennas are operating at 1 GHz. The matching medium used in this system is a glycerine-water mixture. The third prototype system is the one fabricated at Queensland university for imaging intracranial haematomas [35]. This system is comprised of a ring of 16 tapered and corrugated slot antennas, which operate from 1 to 4 GHz. The antennas are in air, without the use of a matching medium. The stroke imaging only relies on the monostatic data (i.e., the reflection coefficient at each antenna). Compared to existing head imaging systems described earlier [5], [13, 14], [33-35], the proposed procedure may be considered a practical alternative to array antennas, due to lower complexity. Specifically, it requires a very simple hardware setup, i.e. one transmitting antenna and one receiving antenna (coupled through a VNA) which rotate in free space around the object to collect the signals in a multi-bistatic fashion. The proposed procedure resorts to HP to detect the variation in dielectric properties between the healthy head tissues and the haemorrhagic stroke. The dielectric properties of the materials used in this paper are a good resemblance of the head tissue properties. The relative permittivity used in the Green's function of eq. (2) has been set to $\sqrt{44.75} \cong 6.7$ in order to meet the impedance matching requirements [36]. In simulations, detection has been achieved both using the subtraction artefact removal and the rotation subtraction artefact removal procedure. In measurements, only the rotation subtraction artefact removal procedure has been used, being the more realistic case in first aid scenario. As highlighted in Fig 11, detection through measurements is achieved at four different phantom orientations. The results shown in this paper, obtained through simulation and measurements in anechoic chamber, pave the way towards the construction and use of a low complexity microwave imaging device for haemorrhagic brain stroke detection, where antennas operate in free-space. The device [37] will be portable, allowing a pre-hospital use. The device will be constituted of two antennas operating in air, embedded in an appropriate cavity, which may have a cylindrically-shaped section. A cavity with a hole which will permit the insertion of the patient's head, lying in supine position, such as in emergency units. The physical appearance of the device can be derived from Fig. 12. The antennas will rotate around the head and measure electromagnetic fields in multi-bistatic fashion from different transmitting and receiving positions. In more details, the microwave imaging device allows to illuminate the head of the patient using electromagnetic fields in the microwave band, with the aim of measuring the correspondent scattered electromagnetic fields and processing the measured fields to obtain an image. Moreover, the safety aspect is a great challenge which developers of medical imaging devices need to face. The patients are in complete safety, as the connected antennas to the dedicated VNA, are operating with very low input power (mW). Another significant aspect that should be considered here, is the estimated cost of the device. The estimated cost may be in the range of tens of thousands of Euros. Finally, the clinical trials on patients with hyperacute stroke will be soon activated to assess the capability of the microwave imaging device to detect patients with haemorrhagic strokes. Fig. 12 presents the physical appearance and dimensions of the device for haemorrhagic brain stroke detection.

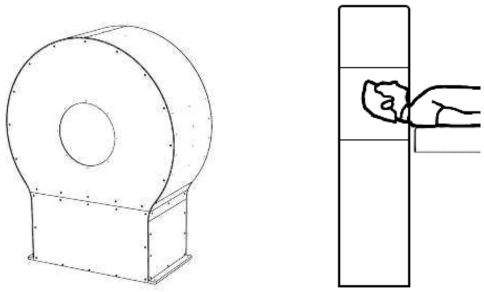

Figure 12: The physical appearance and the dimensions of the device for haemorrhagic brain stroke detection.

5. CRediT statements

Conceptualization, B.S., M.G. and G.T.; methodology, B.S., B.K., N.G. and G.T.; supervision, M.G. and S.D.; validation, B.S., B.K., N.G., M.G., S.D., A.R. and G.T.; writing, original draft preparation, B.S., and N.G.; writing, review and editing, A.R., M.G., S.D. and G.T.

6. Acknowledgments

The project leading to this application has received funding from the European Union's Horizon 2020 research and innovation programme under the Marie Sklodowska-Curie grant agreement No. 793449.
This project has received funding from the European Union's Horizon 2020 research and innovation programme under the Marie Sklodowska-Curie grant agreement No. 872752.
We thank Giovanni Raspa (UBT-Umbria Bioengineering Technologies, Italy) and Michele Scorsipa (UBT-Umbria Bioengineering Technologies, Italy) for providing Fig 12.

References

[1] N. D. Zasler, D. I. Katz, and R. D. Zafonte, Brain Injury Medicine: Principle and Practice, second edition, Demos Medical, New York, (2013).

[2] E. C. Jauch, et al., Guidelines for the early management of patients with acute ischemic stroke: a guideline for healthcare professionals from the American Heart Association/American Stroke Association, Stroke, 44 (3) (2013) 870-947.DOI: https://www.ahajournals.org/doi/10.1161/STR.0b013e318284056a. DOI: https://www.ahajournals.org/doi/10.1161/STR.0b013e318284056a.

[3] D. Ireland and M. Bialkowski, Microwave head imaging for stroke detection, Progress in Electromagnetics Research M, 21 (2011) 163175. DOI:https://doi.org/10.2528/PIERM11082907.

[4] S. Semenov and D. Corfield: Microwave tomography for brain imaging feasibility assessment for stroke detection, International journal of antennas and propagation, (2008).DOI:https:10.1155/2008/254830.

[5] A. Vasquez, et al., First Experimental Assessment of a Microwave Imaging Prototype for Cerebrovascular Diseases Monitoring, IEEE, (2018). DOI: https://doi.org/10.1109/ICEAA.2018.8520397.

[6] B. J. Mohammed, A. M. Abbosh, S. Mustafa, and D. Ireland, Microwave System for Head Imaging, IEEE transaction on Instrumentation and Measurement, 63 (1) (2014). DOI: 10.1109/TIM.2013.2277562.

[7] S. Semenov, Microwave tomography: Review of the progress towards clinical applications, Philos. Trans. A Math. Phys. Eng. Sci, (2009) 3021- 3042. DOI: https://doi.org/10.1098/rsta.2009.0092.

[8] S. Semenov, T. Huynh, T. Williams, B. Nicholson, and A. Vasilenko, Dielectric properties of brain tissue at 1 GHz in acute ischemic stroke: Experimental study on swine, Bioelectromagnetics, 38, no. 2, pp. 158163, 2017.

[9] A.T. Mobashsher, B.J. Mohammed, S. Mustafa, and A. Abbosh, Ultra-Wideband Antenna for Portable Brain Stroke Diagnostic System, 2013 IEEE MTT-S International Microwave Workshop Series on RF and Wireless Technologies for Biomedical and Healthcare Applications (IMWS-BIO), (2013). DOI: 10.1109/IMWS-BIO.2013.6756163.

[10] I. Merunka, O. Fiser, D. Vrba, and J. Vrba, Numerical Analysis of Microwave Tomography System for Brain Stroke Detection, IEEE, (2018), 978-1-5386-2485-2/18. DOI: 10.1109/RADIOELEK.2018.8376398.

[11] V. L. Coli, et al., Detection of Brain Strokes Using Microwave Tomography, IEEE, (2018), 978-1-5386-7102-3/18, DOI: 10.1109/APUSNCURSINRSM.2018.8609404.

[12] M. Klemm, J. A. Leendertz, D. Gibbins, I. J. Craddock, A. Preece, R. Benjamin, Microwave radar-based differential breast cancer imaging: imaging in homogeneous breast phantoms and low contrast scenarios, IEEE Trans. Antennas Propagation, 58 (7) (2010) 2337-2344. DOI: 10.1109/TAP.2010.2048860.

[13] F. Wang and T. Arslan, Assembly of Conformal Antenna Array for Wearable Microwave Breast Imaging Applications, in Antennas & Propagation Conference (LAPC), Loughborough, (2017) 1-4. DOI: 10.1049/cp.2017.0301.

[14] R. Scapaticci, J. Tobon, G. Bellizzi, F. Vipiana, and L. Crocco, Design and Numerical Characterization of a Low-Complexity Microwave Device for Brain Stroke Monitoring, IEEE Transactions on Antennas and Propagation, 66 (12) (2018). DOI: 10.1109/TAP.2018.2871266.

[15] S. Ahsan, M. Koutsoupidou, E. Razzicchia, I. Sotiriou, and P. Kosmas, Advances towards the Development of a Brain Microwave Imaging Scanner, 13th European Conference on Antennas and Propagation, (2019).

[16] L. Chen, L. Xia, H. Li, Sh. Zhang, Sh. Lan, An improved head imaging algorithm based on Huygens Principal, International Symposium on Antennas and Propagation (ISAP), (2018) 1-2.

[17] L. Sani, et al., Novel microwave apparatus for breast lesions detection: Preliminary clinical results, Biomedical Signal Processing and Control, 52 (2019) 257-263. DOI: https://doi.org/10.1016/j.bspc.2019.04.025.

[18] N. Ghavami, P. Probert Smith, G. Tiberi, D. Edwards, and I. Craddock, Non-iterative beamforming based on Huygens principle for multistatic ultrawide band radar: application to breast imaging, IET Microwaves, Antennas & Propagation, 9 (12) (2015) 1233-1240. DOI: 10.1049/iet-map.2014.0621.

[19] A. Vispa, et al., UWB device for breast microwave imaging: phantom and clinical validations, Measurement, 146 (2019) 582-589. DOI: https://doi.org/10.1016/j.measurement.2019.05.109.

[20] N. Ghavami, G. Tiberi, M. Ghavami, S. Dudley, and M. Lane, Huygens principle based UWB microwave imaging method for skin cancer detection, International Symposium on Communication Systems, Networks and Digital Signal Processing (CSNDSP), Prague, (2016) 1-4. DOI: 10.1109/CSNDSP.2016.7573969.

[21] N. Ghavami, G. Tiberi, D. J. Edwards and A. Monorchio, UWB Microwave Imaging of Objects with Canonical Shape,IEEE Transactions on Antennas and Propagation, 60 (1) (2012) 231-239. DOI: 10.1109/TAP.2011.2167905.

[22] N. Seladji-Hassaine and F. T. Bendimerad, Compact Triangular Microstrip Antenna with Fractal Ground, Proc. Academics World 10th International Conference, Istanbul, Turkey, (2015).

[23] A. T. Mobashsher, K. S. Bialkowski, and A. M. Abbosh, Design of Compact Cross-Fed Three-Dimensional Slot-Loaded Antenna and Its Application in Wideband Head Imaging System, IEEE Antennas Wirel. Propag. Lett. 15 (2016) 1856-1860. DOI: 10.1109/LAWP.2016.2539970.

[24] M. Aldhaeebi and I. Elshafiey, New Antenna Design for Hyperthermia Treatment of Human Head, UKSim-AMSS 16th International Conference on Computer Modelling and Simulation, Cambridge, (2014), 96-100. DOI: 10.1109/UKSim.2014.75.

[25] https://itis.swiss/virtual-population/tissue-properties/database/dielectric-properties/.

[26] A. T. Mobasher, A.M. Abbosh, and Yifan Tang, Microwave system to detect traumatic brain injuries using compact unidirectional antrenna and wideband transceiver with verificationon realistic head phantom, IEEE-MTT, 62 (9) (2014). DOI: 10.1109/TMTT.2014.2342669.

[27] S. Symeonidis, W. G. Whittow and C. Panagamuwa, Design and characterization of a three-material anatomical bone phantom for implanted antenna applications, Loughborough Antennas & Propagation Conference, (2017) 1-5. DOI: 10.1049/cp.2017.0253.

[28] P. M. Meaney, C. J. Fox, S. D. Geimer and K. D. Paulsen, Electrical Characterization of Glycerin: Water Mixtures: Implications for Use as a Coupling Medium in Microwave Tomography, in IEEE Transactions on Microwave Theory and Techniques, 65 (5) (2017) 1471-1478. DOI: 10.1109/TMTT.2016.2638423.

[29] G. Tiberi, N. Ghavami, D. J. Edwards and A. Monorchio, Ultrawideband microwave imaging of cylindrical objects with inclusions, in IET Microwaves, Antennas and Propagation, 5 (12) (2011) 1440-1446. DOI: 10.1049/iet-map.2011.0033.

[30] M. Klemm, I. J. Craddock, J. A. Leendertz, A. Preece, and R. Benjamin, Improved delay-and-sum beamforming algorithm for breast cancer detection, International Journal of Antennas and Propagation, (2008), Article ID: 761402. DOI: http://dx.doi.org/10.1155/2008/761402.

[31] E.C. Fear, Xu Li, S.C. Hagness, M.A. Stuchly, Confocal microwave imaging for breast cancer detection: Localization of tumors in three dimensions. IEEE Trans. Biomed. 49 (8) (2002), 812822. DOI: 10.1109/TBME.2002.800759.

[32] M. A. Elahi, M. Glavin, E. Jones, and M. O'Halloran, Artifact Removal Algorithms for Microwave Imaging of the Breast, Progress in Electromagnetics Research, 141 (2013) 185-200. DOI: 10.2528/PIER13052407.

[33] S. Candefjord, et al., Microwave technology for detecting traumatic intracranial bleedings: Tests on phantom of subdural hematoma and numerical simulations, Med. Biol. Eng. Comput., 55 (8) (2017) 1177-1188. DOI: http://dx.doi.org/10.1007/s11517-016-1578-6.

[34] M. Hopfer, R. Planas, A. Hamidipour, T. Henriksson, and S. Semenov, Electromagnetic tomography for detection, differentiation, and monitoring of brain stroke: A virtual data and human head phantom study, IEEE Antennas Propagation. Mag., 59 (5) (2017) 86-97. DOI: 10.1109/MAP.2017.2732225.

[35] A. T. Mobashsher and A. M. Abbosh, On-site rapid diagnosis of intracranial hematoma using portable multi-slice microwave imaging system, 6 (37620) (2016) 37620. DOI: 10.1038/srep37620.

[36] G. Tiberi, N. Ghavami, D. J. Edwards, A. Monorchio, UWB body area network channel modelling: An analytical approach, ELSEVIER, International Journal of Electronics and Communications (AE), (2012). DOI: https://doi.org/10.1016/j.aeue.2012.03.014.

[37] G. Tiberi, R. Raspa, Device for microwave measurement of a dielectric discontinuity of a material, Patent WO 2019 202464 A2, (2018).